NANO LETTERS

2007
Vol. 7, No. 7
2094−2100

Understanding Plasmons in Nanoscale Voids

Robin M. Cole,*,† Jeremy J. Baumberg,*,† F. J. Garcia de Abajo,§ Sumeet Mahajan,‡ Mamdouh Abdelsalam,‡ and Philip N. Bartlett‡

University of Southampton, Southampton, United Kingdom, and Instituto de Optica, CSIC, Madrid, Spain

Received May 4, 2007; Revised Manuscript Received May 31, 2007

ABSTRACT

Metallic nanoscale voids ("anti-nanoparticles") are shown to possess radically different plasmon modes to metal nanoparticles. Comparing new boundary element calculations for the first time with experiment clearly and intuitively identifies plasmon wavefunctions in spherical voids according to their atomic-like symmetries. As the spherical voids are progressively truncated, the degenerate radial modes split in energy, with intense coupling to incident light at specific optimal angles. In contrast to nanoparticles, voids embedded in metal films possess additional rim plasmon modes that selectively couple with void plasmons to produce bonding and antibonding hybridized states with significant field enhancements. These modes, which are verified in experiment, are crucial for the effective use of plasmons in antenna applications such as reproducible surface enhanced Raman scattering.

There is currently intense interest in characterizing and engineering electromagnetic fields in nanoscale structures because structuring a material at this scale results in novel optical properties that are not present for the bulk material.[1−3] In particular, the interaction of light with a metal surface can be controlled by structuring the surface on, or below, the scale of the optical wavelength. Using appropriate coupling techniques,[4,5] incident light becomes bound to the metal surface through its interaction with resonant electronic charge oscillations, resulting in propagating quasiparticles known as a surface plasmon polaritons (SPPs). Furthermore plasmons can be locally trapped on a surface using a nanoscale optical resonator, producing significantly enhanced optical fields at precise locations. While metallic nanoparticles in close proximity or with sharp tips have been the focus of most attention, we have highlighted an alternative nano-*void* plasmon geometry, which is much more controllable and produced in well-defined films.[6] Because the enhanced plasmon fields are desirable for a host of applications, including surface enhanced Raman spectroscopy (SERS)[7] and novel metamaterials, it is critical to understand the nature of the plasmon fields both quantitatively and intuitively.

Plasmon resonators (PRs) have been investigated both experimentally and theoretically.[8] To utilize these structures for applications, it is important to know the energies, coupling strengths, and field profiles of the different modes that exist. Analytical solutions to the modes of PRs have been found in only a few cases, including homogeneous[9] and multilayered spheres,[10] ellipsoids, and infinitely long circular cylinders.[11] These examples of generalized Lorenz−Mie theory require specific symmetrical particle shapes and are generally treated as isolated from each other and any conducting substrate. Such idealized structures are often difficult to realize in experiment, particularly for large-scale reproducible fabrication.

While much work concentrates on nanoparticles and cylindrical holes,[12] rather little is known about the plasmonic modes of 3D voidlike nanostructures that offer a number of compelling advantages for exploitation. Voids in metals can be embedded in substrates that are easy to handle, they can be produced very controllably using thin-film growth without nanolithography, they offer large field enhancements, are well-coupled to incident light in comparison to nanoparticles, and they can be systematically studied using angle-dependent spectroscopy. One structure that we have recently extensively fabricated and studied is the truncated spherical nanocavity.[6,13,14] The advantage of utilizing this geometry is that spherical nanovoids can be simply made, finely controlled, and give broad spectral tuning of plasmon modes. Such a structure is shown in Figure 1a and is produced by a self-assembly and templating procedure.[15] Structures can be graded in thickness across a substrate, allowing rapid investigation of the effects of shape on the observed plasmon modes as they evolve from open periodic dish structures up to fully encapsulated spherical cavities. Reflectivity measurements (Figure 1b) reveal strong absorption lines in the visible and near-infrared (NIR) spectra due to void plasmon modes

* To whom correspondence should be addressed. E-mail: rmc3@phys.soton.ac.uk (R.M.C.); baumberg@phys.soton.ac.uk (J.J.B.).
† School of Physics and Astronomy, University of Southampton.
‡ School of Chemistry, University of Southampton.
§ CSIC.

10.1021/nl0710506 CCC: $37.00
Published on Web 06/14/2007

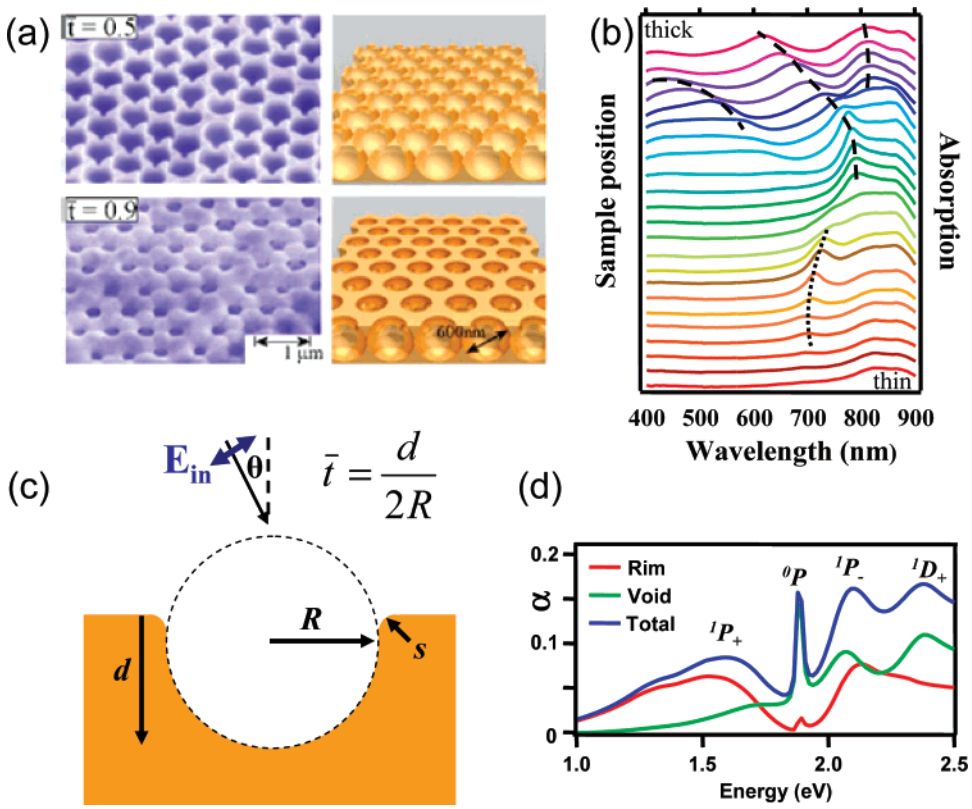

Figure 1. (a) SEM images (left) and morphologies (right) of 600 nm diameter Au spherical void structures, at normalized cavity thickness $\bar{t} = 0.5, 0.9$. (b) Experimental absorption spectra from a nanovoid structure which is graded in thickness from $\bar{t} = 0.1$ (top) to $\bar{t} = 0.95$ (bottom). Dashed lines indicate void plasmon modes inside the cavities, and the dotted line an SPP surface mode. (c) Parametrization scheme for void cavity of radius R, with metal thickness d and rim rounding curvature s. (d) Theoretical absorption spectra of a void of $R = 250$ nm, $\bar{t} = 0.925$ and angle of incidence 60°, separated into components from rim region and interior of void. Mode labeling is described in the text.

localized inside the cavities as well as SPP propagating modes on the surface of the structure (which have been fully characterized elsewhere).[14]

In this paper, we present for the first time a method to theoretically characterize the plasmon energies and fields of localized modes in void structures, including their optical coupling and their mode symmetries, using the spherical nanovoid as a prototype. By moving beyond fully spherical symmetry toward realistic structures, the influence of real corners, rims, and folded architectures can be studied on the plasmons' confinement and their coupling to incident light. This allows quantitative comparison both with extensive experiments and with primitive models in order to build an intuition for the plasmonics of voids. This knowledge is essential in order to design metallic nanostructures that couple light to molecular-scale dipoles for plasmon-enhanced Raman scattering, photoluminescence, photoconductivity, and optically nonlinear devices.

We first introduce the electromagnetic modes within *completely* metal-encapsulated spherical voids. The Mie solutions to Maxwell's equations describe the electromagnetic scattering from a sphere of arbitrary size. Resonant solutions depend on the size of the sphere and on the dielectric function of the sphere and its surrounding environment. These general Mie solutions allow calculation of the modes of a spherical cavity within an infinite expanse of metal.[16,13] For small spheres ($kR \ll 1$, where k is the wave vector of incident light), the quasistatic solutions $\omega_l = \omega_p^{2D}\sqrt{(L+1)/(2L+1)}$ are pushed above the SPP depending on the number of radial nodes, L. As the void size increases, retardation effects modify the mode energies, mixing SPPs with Fabry−Perot cavity modes to produce a new class of void plasmons. These plasmon states resemble atomic orbitals with spherical harmonic components $Y_{L,m}$ incorporating a vectorial character. However, because this model has the voids completely embedded inside the metal, it is not possible to understand how such modes are out-coupled, nor is it possible to directly compare with the corresponding inverse nanoparticle structure. This makes comparison with experimental data on truncated void cavities at best qualitative. Without the predicted field distributions excited by different angles of incidence, it is impossible to explain molecular emission or molecular Raman scattering inside such voids.

Currently, neither full 3D electromagnetic solvers nor analytic calculations can make any headway in realistic optical modeling of these 3D nanostructures. Using a boundary element method (BEM),[17] we have devised a computationally efficient solver for cylindrically symmetric structures, using adaptive meshing to provide appropriate spatial resolution in different regions. In the BEM model, the field inside a single isolated cavity is expressed in terms of the charges and currents of the structure surface. The

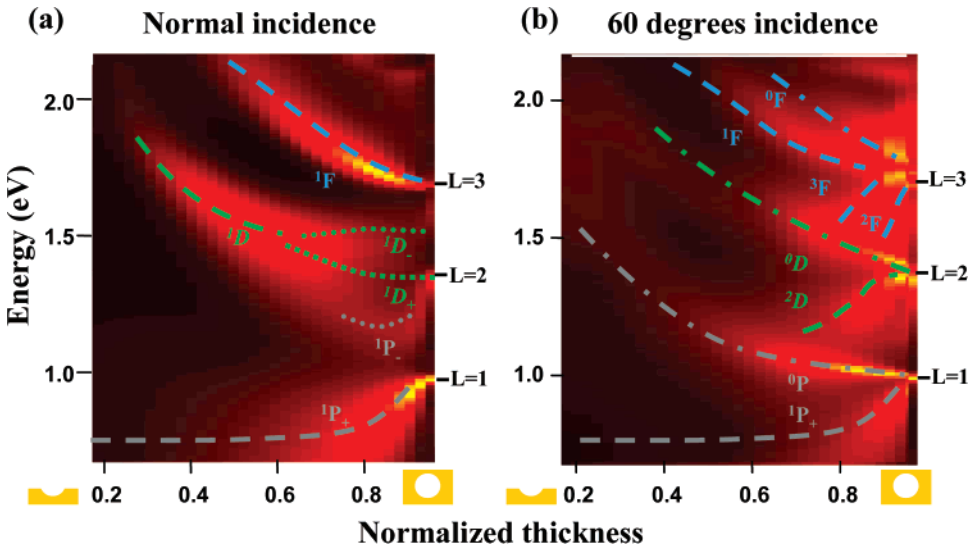

Figure 2. (a) Model normalized absorption for $R = 500$ nm Au voids at (a) normal incidence and (b) 60° for increasing film thickness. Dashed lines are guides to the eye, with labeling described in text.

boundary conditions provide a set of linear integral equations in these charges and currents that are decomposed in terms of each azimuthal $\exp(im\varphi)$ component. Because coupling between different m components is forbidden, their solutions can be analyzed independently despite mixing of the L components.

It is instructive to view the truncated solutions as they develop from the initial spherical void solutions. We adopt the mode labeling ${}^mL = {}^{0,1,\cdots}P,D,F$, where the $L = 0$ mode is forbidden from symmetry arguments. Illuminating the single cavity embedded in a surface with a plane wave at a particular angle of incidence and polarization allows us to extract the 3D optical field distribution at each energy as well as the local absorption and Poynting vectors at the metal surfaces. Full frequency-dependent dielectric functions are used for both dielectric and metallic components. Although we model only individual void cavities rather than a hexagonal array, angular mapping experiments have shown that coupling between neighboring cavities is weak.[6] To parametrize the truncated void structure (Figure 1c), we define the normalized thickness as $\bar{t} = d/2R$, where d is the planar metal thickness and R is the spherical void radius which experimentally is varied from 150 nm to many micrometers. Typically, we focus on illumination at visible and near-IR wavelengths from 400 nm to 2 μm, corresponding to experiment. We use a rounding of the upper rim $s = 10$ nm although, crucially for reproducibility and quantisation, we find the mode absorptions and field profiles to be rather insensitive for $s < 100$ nm.

The absorption for a 250 nm radius cavity, thickness $\bar{t} = 0.92$ and incident angle 60° is shown in Figure 1d, correctly normalized to be directly comparable with the hexagonal array. The absorption profile reveals several modes, not predicted by the Mie equations. Their assignments (discussed below) are based on the decomposition into azimuthal m components and the evolution from the well-defined L-states at $\bar{t} = 1$. While some modes have a narrow spectral width (such as ${}^0P$ with fwhm = 45meV), others exhibit broadband excitation (such as ${}^1P_+$ with fwhm = 250meV). This arises from the excitation of strong *rim dipole modes* associated with charge buildup at the void rim for $\bar{t} > 0.6$. This rim mode has $m = 1$ symmetry and will couple only to void modes with $m = 1$ of the same energy, resulting in mixed mode configurations with strongly enhanced fields.[18,19] We denote the two hybridized modes associated with the coupling between ${}^1P$ and the rim as the lower energy, bonding mode (${}^1P_+$), and higher-energy, antibonding (${}^1P_-$) mode. We confirm that such coupled rim-void modes do not exist in the corresponding inverse nanoparticle structures. By identifying the absorption from different m states, and from different spatial regions of the metal surface, the origin of the different modes can be explored.

While experiments clearly show the tuning of the mode energies as the spherical cavity is progressively truncated (Figure 1b), only intuitive models have yet offered an explanation.[14] The negatively curved void surface localizes the electromagnetic energy in an enclosed region, with higher-order modes increasingly localized at the metal surface. As the structure is increasingly truncated, the modes are less encapsulated and most of them move away from the metal. Hence the modes increase in energy as truncation proceeds. Approaching from the opposite limit, the modes at low $\bar{t}$ must resemble the 2D SPP dispersion, with the small dimples leading to progressively more plasmon localization, initially as in a photonic or plasmonic crystal. Hence, in general, we expect modes to drop out of the SPP bands toward the Mie solutions as $\bar{t}$ increases.

Using the BEM model, we illustrate the actual thickness behavior in detail in Figure 2 through the absorption spectra of incident light at both normal incidence and 60°. A rich variety of modes are observed that display a strong energy dependence on the structure morphology. While the modes are strongly dependent on the dimensions of the cavity, all the representative phenomena of note are exemplified for the 500 nm radius cavity shown. On the right side are indicated the $L = 1,2,3$ Mie solution energies in the

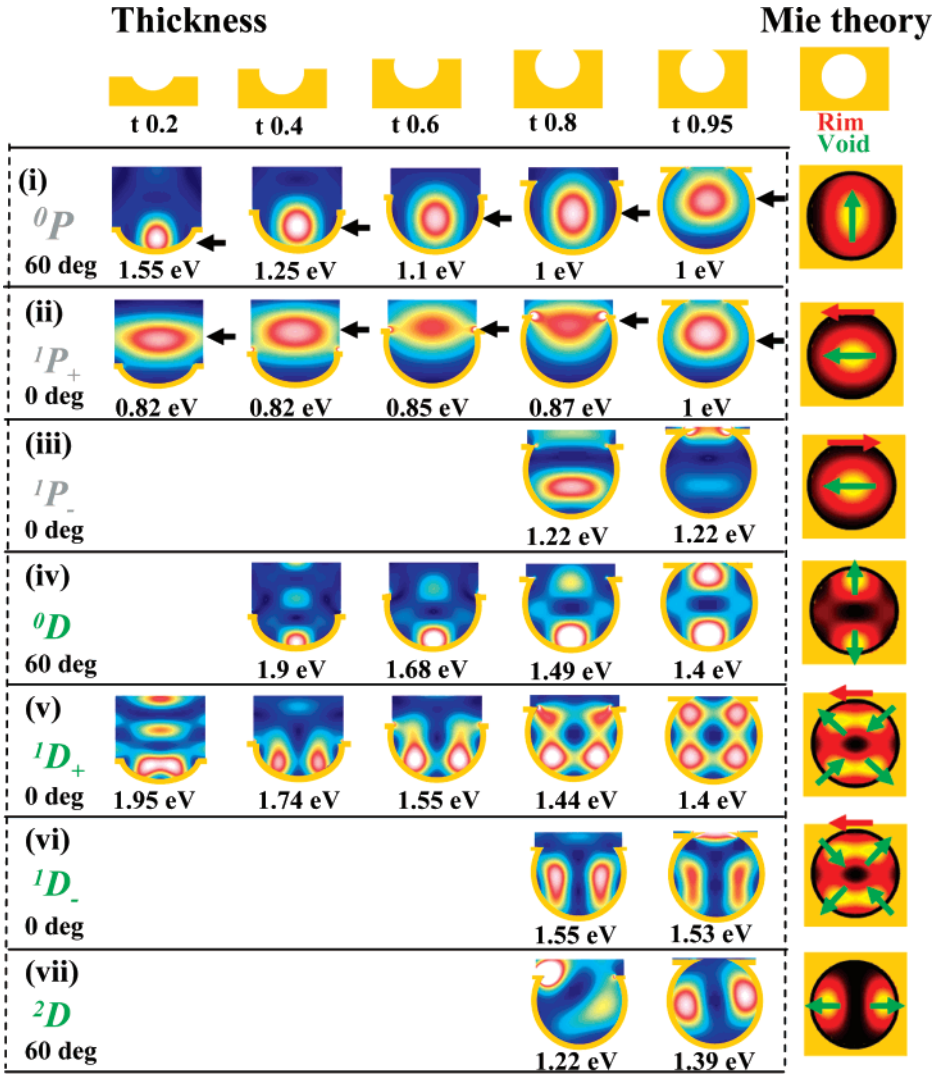

Figure 3. Spatial intensity distributions at increasing thickness, with (right) field profiles from Mie theory. Vertical position of the maximum optical field for the $^1P_+$ and ^0P modes with increasing $\bar{t}$ indicated by black arrows. Field orientations for rim (red) and void (green) modes indicated by arrows.

equivalent full spherical cavity. Clearly evident is the way that these modes split and evolve in energy as the thickness decreases. Near $\bar{t} = 1$, the modes spectrally sharpen and become isolated from the incident light, matching in detail the Mie solutions.

By examining (Figure 3) the spatial field distributions $|E(r)|^2$ for specific m components, the different modes can be identified. The spatial field distribution and vector orientation of each Mie solution (plotted on right-hand side) show which truncated mode they clearly correspond to. Low-m modes have optical fields closer to the central z-axis of the void, in less contact with the metal surface. The field vector orientations give a clear understanding of the angle dependence: while modes with $m = 0$ have vertical field alignment that cannot couple to normally incident light, in contrast, $m = 1$ modes are well coupled at normal incidence.

The sharpest low-energy mode is the ^0P, which is only seen for $\theta > 0°$ (gray, Figure 2b). As the full spherical cavity is truncated, the charge distribution of this mode at the top of the void is strongly perturbed and hence the mode energy rapidly rises (Figure 3i). As the thickness reduces further, the optical coupling to this mode weakens and it draws closer to the metal surface. For low $\bar{t}$, the ^0P turns into a standing wave of propagating SPPs which are tethered to the shallow dishes. The tight field distribution and poor symmetry match to incident light mean that this mode is not well coupled for absorption at small thicknesses.

On the other hand the ^1P mode shows a very different behavior (Figure 2a). This mode energy splits immediately the cavity is truncated. As mentioned already, this is because the mode strongly couples to the rim dipole mode. The resulting low-energy $^1P_+$ bonding mode has field vectors of void mode and rim mode that are parallel (Figure 3ii). On the other hand, the higher-energy antibonding $^1P_-$ mode has antiparallel alignment of these field vectors (Figure 3iii), which causes it to have very weak coupling to incident light. As the cavity is further truncated, the $^1P_+$ mode drops to a fixed energy and loses its absorption strength. This is because the mode rises above the metal surface and eventually at low $\bar{t}$ corresponds to the interference standing wave of

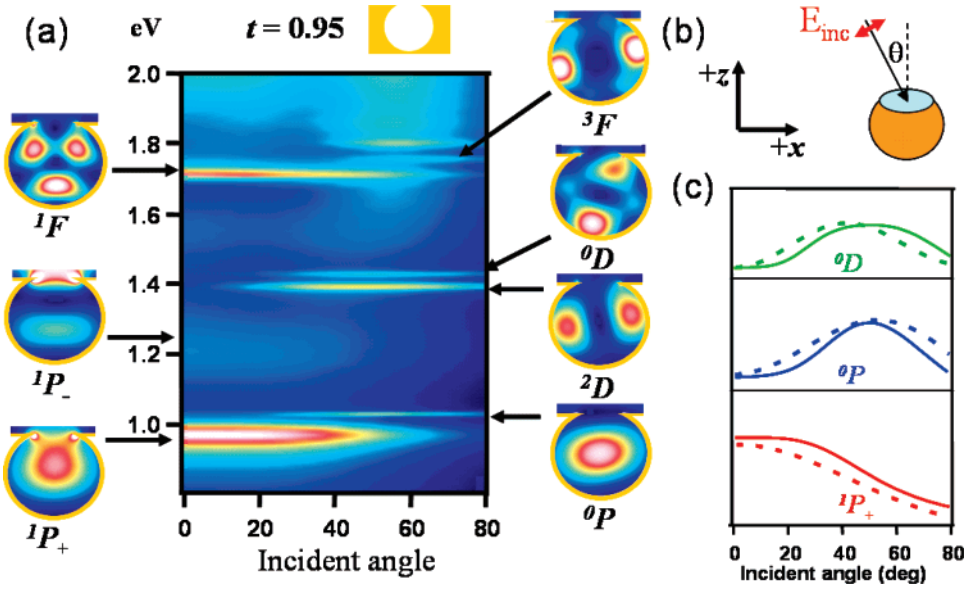

Figure 4. (a) Angle-dependent absorption of $R = 500$ nm cavity at $\bar{t} = 0.95$ together with selected $|E|^2$ field plots. (b) Orientation of incident light onto void and rim gives (c) observed absorption vs angle of the P and D modes. Theory lines (dashed) described in text.

incoming and reflected light, which has a field null at the metal surface. The contrasting positions of field maxima within the cavity for the $^1P_+$ and ^0P modes (arrows in Figure 3) show the key role of the rim in attracting and repelling the light fields to and from the metal surface. Because the $^1P_+$ mode has a strong rim component, it is sensitive to the rim shape and height and only loses absorption strength as the void mode moves further above the rim height.

A similar type of behavior is seen for the $L = 2$ modes (green dashed lines in Figure 2). While the ^1D mode again exhibits strong coupling to the rim mode, near-degeneracy with the $^1P_-$ mode gives further mixings, creating three broad mixed modes for $\bar{t} > 0.6$. For $\bar{t} < 0.6$, the ^1D mode dominates the spectrum: the skewed vector alignment of the two strong field lobes close to the metal surface either side of the void bottom (Figure 3v) gives it good symmetry overlap with $m = 1$ incident light. For $\bar{t} > 0.7$, this mode resembles a whispering gallery mode.[20] On the other hand, for small $\bar{t}$, this mode resembles the interferometric standing wave, but with a phase shift that brings it very close to the metal surface. Hence this mode plays a strong role in efficiently feeding electromagnetic energy into molecules or nanoparticles on the metal surface. At normal incidence, the $m = 0$ mode is not coupled due to its vertical field orientation, while the $m = 2$ mode is also not seen because of its back-to-back field orientation (Figure 3vii). Once again, the $m = 0$ mode has associated charge maxima situated right at the top of the void and is most perturbed by the initial truncation. Eventually, on further truncation, the ^0D mode becomes the second-order SPP mode, while the ^2D mode disappears. A similar story is repeated with the $L = 3$ modes (blue dashed lines in Figure 2), with the ^1F mode absorption dominating at normal incidence.

To summarize, the L spherical void modes are split by truncation into a number of m states, whose energy tuning with thickness depends closely on the field distribution of each mode. The $m = 1$ modes are further strongly coupled to the void rim, producing lower-energy bonding states that couple well with incident light. Precisely where absorption takes place on the metal surface is set by the mode numbers, the angle of incidence, and the mode geometry in nontrivial ways.

Experimental spectra reveal a strong angle dependence of the absorption from the low L void modes. Although nondispersive (the lack of energy dependence on angle of incidence is indicative of their localized spatial extent), the modes preferentially absorb at particular incident angles. To compare with theory, field distributions are tracked in the BEM model for different angles of incidence of TM/TE light for the 500 nm radius void at a thickness $\bar{t} = 0.95$ (Figure 4a). The m-dependent coupling is clearly resolved, with angle-dependent absorptions for the ^0P, $^1P_+$, and ^0D modes extracted in Figure 4c. The narrow spectral line width of the ^0P mode is ascribed to its lack of radiative coupling to the rim, which both decreases its total absorption strength and hence radiative decay, and its penetration into the metal and hence current-induced heating. The absorption matches the expected angular overlap of the incident and void-mode fields in the far field radiation zone[21] (dashed lines) with an additional $\cos(\theta)$ falloff due to the reduced area viewed by an angled incident beam: for the ^0P, this goes as $[\sin^2(\theta)]\cos(\theta)$ and the ^0D goes as $[\sin^2(\theta)\cos^2(\theta)]\cos(\theta)$. By contrast, the ^1P follows a $[1 + \cos^2(\theta)]\cos(\theta)$ angle dependence. At normal incidence, only $m = 1$ modes are excited: the $^1P_+$ mode is strongly coupled due to its interaction with the radiative rim mode, while the $^1P_-$ is almost invisible. As the angle of incidence is increased, the strength of coupling between void and rim mode is modified, with a maximum coupling at 25°. One result of these dependences is that, in an optical microscope configuration, for a typical 20× objective with NA = 0.2, *only* the $m = 1$ modes are observed. The intrinsic angle-dependent coupling

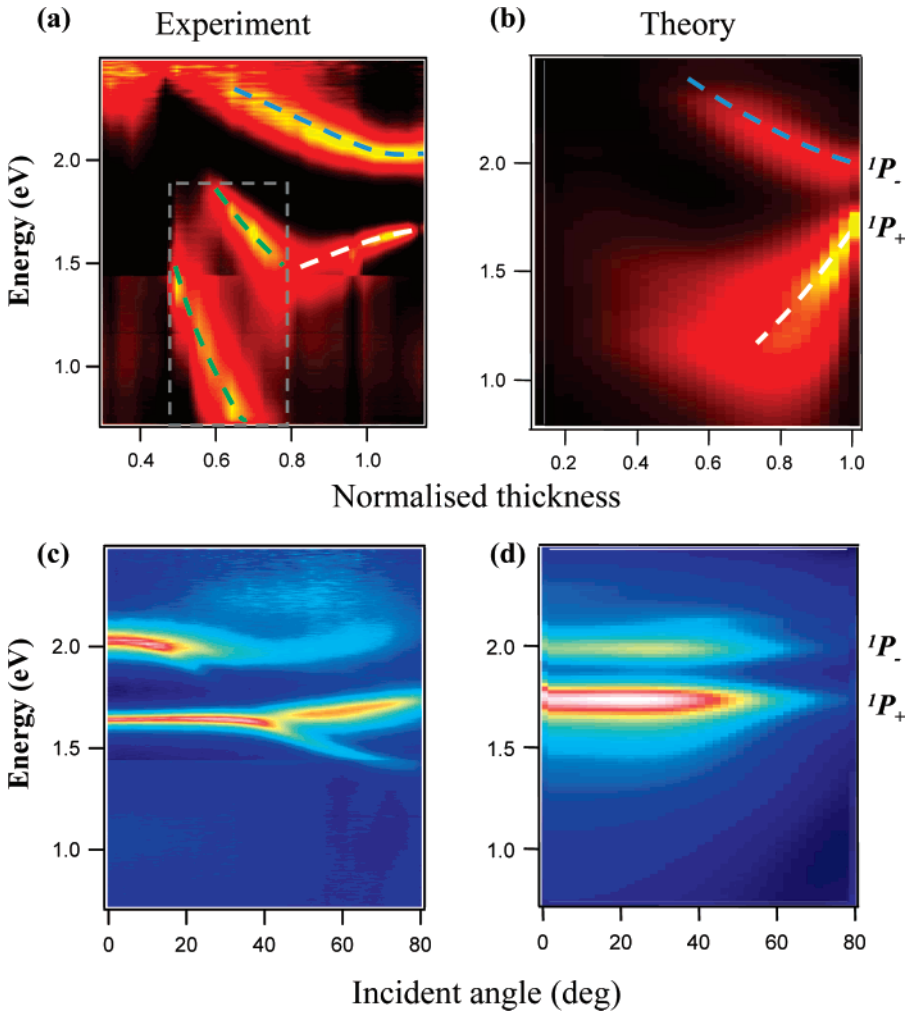

Figure 5. (a) Measured and (b) calculated absorption for $R = 250$ nm cavity structure graded in thickness from thin (left) to thick (right) at $\theta = 0°$ (lines track plasmon modes). (c) Experimental and (d) calculated dispersion for the structure near full encapsulation, $\bar{t} = 0.99$.

to these modes has significant implications for the applications of these nanostructures, for example, as substrates for SERS in typical microscope geometries.

Our samples are comprehensively studied using reflectivity measurements taken on an automated goniometer covering $\{\bar{t} = 0-1, \theta = 0-80°\}$.[6] Experimental reflectivity measurements for a $R = 250$ nm cavity structure graded in thickness are compared with calculation in Figure 5. For this structure, there are few modes, widely separated in energy, allowing their precise characterization. At $\theta = 0°$ (Figure 5a), two distinct high-energy plasmon modes red-shift for increasing thickness, while an extra low-energy mode around $\bar{t} = 0.5$ (dashed box) is discussed later. The first mode (white) rises in energy for $\bar{t} > 0.8$ and comparing with calculation (Figure 5b) is identified as the $^1P_+$ mode. The second mode (blue) drops monotonically in energy with $\bar{t}$, matching with the theory prediction of the $^1P_-$ mode; its strong absorption is due to increased $\mathcal{I}m(\epsilon_{Au})$ at shorter wavelengths. The ^0P mode is not observed in the experimental data.

Several differences between the experimental and simulated structures complicate comparison. The real periodic array of voids supports standing wave SPP modes with plasmonic bandgaps for $\bar{t} < 0.4$ and also for $\bar{t} > 0.9$, ignored here and analyzed elsewhere.[14] A second difference are small holes into the top of the voids even for $\bar{t} = 1$ due to geometry-limited electrochemical growth. Therefore, the voids are never completely encapsulated, inhibiting the development of $m = 0$ modes and modifying higher m modes (hence the discrepancy for $^1P_+$). Third, for $\bar{t} \approx 0.5$, the appearance of a low-energy mode coincides with the formation of small holes between neighboring voids (green). The hole reconnects around $\bar{t} = 0.65$, forming bowtie-shaped features above circular windows between the voids. This mode also perturbs the $^1P_+$ mode and is under further investigation. The experimental and theoretical angular dispersion for the structure near full encapsulation (Figure 5c,d) supports our identifications. Also experimentally visible is mixing of the propagating SPPs with the localized void modes. Coupling is observed between the SPP and the $^1P_+$ mode, resulting in the splitting above 45°, while the SPP mode also enhances coupling to the $^1P_-$ mode.[20]

In conclusion, we have shown an accurate theoretical model that reveals the absorption and fields of resonant plasmonic modes inside azimuthally symmetric metallo-dielectric nanostructures. Using the example of a spherical void whose modes are well understood, the behavior of real

modes in truncated structures is identified and shown to differ strongly from nanoparticles. We believe that the symmetry arguments used in our discussions are rather general and thus apply to more general void configurations (for instance, we have confirmed these general behaviors in conical pits). In particular, the coupling of void plasmons with rim dipoles is of crucial importance. We identify several classes of modes with plasmonic field at the metal surface (and hence capable of exciting dipoles in deposited molecules or nanoparticles) that dominate in different specific geometrical regimes.

Acknowledgment. This work was supported by EPSRC grant EP/C511786/1.

Note Added after ASAP Publication. This paper was published ASAP on June 14, 2007. A name in the author institution list was updated. The revised paper was reposted on June 18, 2007.

References

(1) Barnes, W. L.; Dereux, A.; Ebbesen, T. W. *Nature* **2003**, *424*, 824−830.
(2) Smith, D. R.; Pendry, J. B.; Wiltshire, M. C. K. *Science* **2004**, *305*, 788−792.
(3) Ozbay, E. *Science* **2006**, *311*, 189−193.
(4) Otto, A. *Z. Phys.* **1968**, *216*, 398.
(5) Ritchie, R. H.; Arakawa, E. T.; Cowan, J. J.; Hamm, R. N. *Phys. Rev. Lett.* **1968**, *21*, 1530−1533.
(6) Kelf, T. A.; Sugawara, Y.; Baumberg, J. J.; Abdelsalam, M.; Bartlett, P. N. *Phys. Rev. Lett.* **2005**, *95*, 116802.
(7) Kneipp, K.; Kneipp, H.; Itzkan, I.; Dasari, R. R.; Feld, M. S. *J. Phys. C.* **2002**, *14*, R597−R624.
(8) Wang, H.; Brandl, D. W.; Nordlander, P.; Halas, N. J. *Acc. Chem. Res.* **2007**, *40*, 53−62.
(9) Mie, G. *Ann. Phys. (Leipzig)* **1908**, *25*, 377.
(10) Aden, A. L.; Kerker, M. *J. Appl. Phys.* **1951**, *22*, 1242.
(11) Gouesbet, G.; Grehan, G. *Part. Part. Syst. Charact.* **1994**, *11*, 299−308.
(12) Degiron, A.; Lezec, H. J.; Yamamoto, N.; Ebbesen, T. W. *Opt. Commun.* **2004**, *239*, 61−66.
(13) Coyle, S.; Netti, M. C.; Baumberg, J. J.; Ghanem, M. A.; Birkin, P. R.; Bartlett, P. N.; Whittaker, D. M. *Phys. Rev. Lett.* **2001**, *87*, 176801.
(14) Kelf, T. A.; Sugawara, Y.; Cole, R. M.; Baumberg, J. J.; Abdelsalam, M.; Cintra, S.; Mahajan, S.; Russell, A. E.; Bartlett, P. N. *Phys. Rev. B* **2006**, *74*, 245415.
(15) Bartlett, P.; Baumberg, J. J.; Coyle, S.; Abdelsalam, M. *Faraday Discuss.* **2003**, *125*, 117.
(16) *Electromagnetic Surface Modes*; Boardman, A. D, Ed.; Wiley: Chichester, U.K., 1982.
(17) Garcia de Abajo, F. J.; Howie, A. *Phys. Rev. Lett.* **1998**, *80*, 5180−5183.
(18) Kim, J.; Liu, G. L.; Lu, Y.; Lee, L. P. *Opt. Express* **2005**, *13* 8332−8338.
(19) Cortie, M.; Ford, M. *Nanotechnology* **2007**, *18*, 235704.
(20) Cole, R. M.; Sugawara, Y.; Baumberg, J. J.; Mahajan, S.; Abdelsalam, M.; Bartlett, P. N. *Phys. Rev. Lett.* **2006**, *97*, 137401.
(21) *Classical Electrodynamics;* Jackson, J. D., Ed.; Wiley: Chichester, U.K., 1998.

NL0710506